fluids

Article

Investigation of Microjet Engine Inlet Pressure Distortions at Angled Inflow Velocity Conditions

Santiago Sanchez Villacreses, Jun Yao *, Yufeng Yao and Budi Chandra

School of Engineering, College of Art, Environment and Technology, University of the West of England (UWE), Bristol BS16 1QY, UK; santiago2.sanchezvillacreses@live.uwe.ac.uk (S.S.V.); yufeng.yao@uwe.ac.uk (Y.Y.); budi.chandra@uwe.ac.uk (B.C.)
* Correspondence: jun.yao@uwe.ac.uk

Abstract: The Armfield CM14 microjet axial flow turbine engine has been tested in open space at ambient conditions with engine inlet pressure at the aerodynamic interface plane (AIP) measured by a built-in pressure sensor for validating computational fluid dynamics (CFD) studies. A three-dimensional computational domain of the test engine intake duct configuration is defined, followed by mesh convergence studies. The latter results in a fine mesh of 5.7 million cells on which CFD-predicted engine inlet pressures are in good agreement with the experimental measurements at the AIP face for 20–100% throttles. CFD studies are continued to investigate the engine inlet pressure distortions at two inflow velocities of 35 m/s and 70 m/s, and various inflow angles ranging from 0° to 30° with a step of 5°, to evaluate their impacts on engine inlet pressure distortions. It is found that pressure distortions increase with the inflow angle, with severe pressure distortions occurring at higher inflow angles above 15°. At the same flow conditions of inflow angle and velocity, pressure distortions from an intake with a flat lip are overall higher than those of a bell-mouth round lip. This is primarily due to a rapid geometry change at the intake entrance causing large vortical flow motions, accompanied by local flow separations at higher inflow angles, therefore impacting the downstream flow field towards the engine inlet.

Keywords: microjet engine; computational fluid dynamics; inlet pressure distortions; flat lip and bell-mouth round lip; aerodynamic interface plane

check for updates

Academic Editor: D. Andrew S. Rees

Received: 7 January 2025
Revised: 3 February 2025
Accepted: 10 February 2025
Published: 13 February 2025

Citation: Sanchez Villacreses, S.; Yao, J.; Yao, Y.; Chandra, B. Investigation of Microjet Engine Inlet Pressure Distortions at Angled Inflow Velocity Conditions. *Fluids* **2025**, *10*, 49. https://doi.org/10.3390/fluids10020049

1. Introduction

Engine inlet flow distortions have significant effects on modern aircraft engine design where a complex intaking system is required to provide a quality and controlled airstream flowing into the engine fan or compressors, and therefore, maintain the overall engine efficiency to ensure engine operability, performance, and durability [1]. Flow distortion can be induced by undesirable aerodynamic flow behaviours such as flow separation, vortex shedding, local secondary flow, boundary-layer ingestion, etc. [2]. These unusual flow behaviours will cause significant levels of perturbation on pressure and temperature fields, or swirling flows due to large flight angles and/or strong crosswinds [3]. Recently, engine inlet pressure distortion has received significant attention from researchers as non-uniformly distributed engine inlet flow can influence the limit of engine stability and degrade the engine performance, along with other environmental concerns, such as higher CO_2 and NO_x emission levels causing contamination.

At a given operation condition, engine inlet pressure distortion can be determined by evaluating the radial and/or circumferential perturbations at the aerodynamic interface plane (AIP) just ahead of the engine fan/compressor entry [4] to provide an indicator of distortion level due to local separated flow and/or strong secondary flows. These flow phenomena often co-exist, and the interactions between them can create even more complicated flow features that are very difficult to interpret due to the coupling effects of the overall variations in the distortion [5,6]. Despite these factors, it is crucial to understand steady-state flow distortion intensity and its extent, because it will have major impacts on the surge margin reduction of a given jet engine propulsion system [4]. Rademakers, Bindl and Niehuis [7] carried out experimental investigations of total pressure distortion effects on the performance of low-pressure compressors of an aero-engine. They noted that there were linear trends in the circumferential distortion coefficient (using a distortion descriptor DC60) and circumferential distortion index (CDI) with total pressure loss at the AIP and a decrease in surge margin. It was thus believed that the variation in pressure recovery at the AIP face due to total pressure loss can have a significant impact on the desirable pressure ratio delivered by the compressor stage [1].

Previous studies have also found that an integrated intake shape can have a large impact on the quality and performance of flow behaviours throughout the entire intake ducting regime till the engine inlet, causing flow distortions at the AIP face [7]. For example, an *S*-shaped intake can induce high flow instability due to secondary flow and flow separation at the intake lip region, leading to large deviations of the local flow from its average mean flow field [5,8]. Moreover, higher total pressure loss has been predicted in *S*-shaped ducts for both inflow at certain incident angles and along the axial flow direction [7]. For an angled inflow, the development of the maximum recovering pressure at the AIP face, induced by adopting a curved intake, e.g., a bell-mouth air meter with a short duct component to guide inflow along the axial direction, does not see a significant improvement for engine spool speed increases up to 100%. This is because the inflow at a non-zero incident angle can still cause some pressure losses with an increase in engine spool speed.

Several descriptors have been proposed and used to quantify the inlet flow distortions. A distortion coefficient using the worst circumferential distortion range of 60° (namely DC60 thereafter), initially derived by Rolls-Royce [9], has been widely used in the UK and Europe to quantify flow distortion levels at the AIP face. Other descriptors, such as circumferential distortion intensity and radial distortion intensity (RDI), are also used as an indication of the magnitude of total pressure defects around the entire ring of the AIP face and the percentage of average pressure differences at the AIP face, respectively. While another distortion index (DI) can be used to measure the extensive pressure differences at the AIP face, it cannot distinguish the pressure variations between the circumferential and radial directions, and it is thus less sensitive to the change in intake mass flowrate and intake duct diameter [10].

Recently, numerical methods such as computational fluid dynamics (CFD) have been widely adopted to investigate the effect of flow distortions on engine inlet fan/compressor performances. CFD work carried out by Hodder [11] and Kennedy et al. [12] investigated engine intake flows at high incident angles. Their studies modelled a full three-dimensional (3D) geometry domain, and key flow features such as attenuation of the engine inlet flow distortions and upstream flow redistributions were successfully captured by the simulations. Carnevale et al. [13] investigated flow separation, induced by interactions between the engine intake duct and downstream fan blades, using both steady and unsteady Reynolds-Averaged Navier–Stokes (RANS) along with turbulence models. They have concluded that the flow distortions can be reduced by tuning the fan blades' orientation to the incoming flow incident angle for both an isolated and/or a powered intake configuration. Iek and Boldman [14] applied a screen boundary condition method in their numerical simulation to investigate the intake duct and engine fan blade interactions due to the change in flow incident angle, by introducing a blockage to the incoming flow, thus replicating real physical effects. They found that the flow blockage is able to suppress some degrees of flow distortions under the condition where flow separation occurs. The CFD study by Peters et al. [15] concluded there is a trade-off between the intake duct length and inflow Mach number for achieving the optimal performance of engine fan blades. Cao et al. [16] carried out CFD simulation by applying a simplified intake-fan model using both steady and unsteady RANS simulations. Their results indicate that the downstream fan face played a critical role in suppressing the flow distortion at the AIP face, and the CFD-predicted DC60 values increased with the increase in inflow incident angles. However, there is a significant increase in the distortion level after a critical incident angle, due to large flow separation observed around the intake lip region. This causes a stall where the flow is massively detached from the intake duct walls.

Some experimental tests have also shown that the engine inlet is able to operate at a low level of flow distortion by decoupling the intake duct from the downstream engine inlet [17]. Experimental tests by Boldman, Iek and Hwang [18] found that rotating propellers could delay flow separation by increasing the incident angle at an intake between 2.7° and 4°, compared to an intake without rotating propellers. This incident angle change is dependent on the operating mass flowrate. Naseri et al. [3] experimentally investigated the total pressure distortion due to steady-state inflow affecting the performance of a microjet gas turbine engine, coupled with an inlet simulator to produce specific flow distortion features at the engine inlet. Their results showed that the engine performance was degraded with an increase in distortion intensity and its extent, with the maximum distortion intensity determined at DC180 (i.e., using circumferential descriptor over a range of 180°). Pecinka et al. [19] performed an experimental investigation on a jet engine based on total pressure distributions at the AIP face to evaluate the effect of different distortion descriptors, i.e., CDI, RDI, DI, DC60 etc., and they found that DC60 can be used to determine flow distortion between different applications without knowing the exact inflow velocity, as DC60 is more independent of mass flowrate, compared to other distortion descriptors that are significantly changed with the inflow mass flowrate. Their experiments were conducted using several types of screens by simulating different flight conditions to replicate flow separations or wake for the intake at higher angles of attack. Their study showed that increased screen density has a significant effect on flow distortion by increasing the inflow turbulence intensity, thus resulting in high pressure distortions at the AIP and downstream fan blade faces.

In this paper, pressure distortion at the AIP face of a microjet turbine engine inlet will be investigated by CFD simulations at various flow incident angles from 0° to 30° at 5° increments, and two flow velocities of 35 m/s and 70 m/s, respectively. The experimental test is carried out using an Armfield CM14 microjet gas turbine engine, fired at 20–100% throttles at ambient conditions in an open space with the pressure at the AIP measured by a built-in sensor for validating CFD predictions. The engine inlet pressure distortion will be characterised by distortion descriptor DC60. Both the original flat lip intake and re-designed bell-mouth round lip intake will be investigated to understand the attenuation of the intake shape effect on flow distortion at the engine inlet ahead of the fan/compressor blade face. CFD simulation will review the pressure distortion at the AIP face of the engine inlet, which could potentially have significant negative impacts on the overall engine performance.

2. Methodology

2.1. Experimental Test Setup

The Armfield CM14 microjet turbine engine [20] (see Figure 1) is a self-contained compact Olympus HP E-start turbine engine [21], comprising a single-stage radial compressor, an annular combustion chamber and a low-mass, high-performance axial turbine designed to demonstrate the principle and characteristics of an aeronautical engine. A high-precision fuel gear pump is employed to induce a fast engine response. The engine can reach a maximum speed of 105,000 rpm, and a built-in software control system provides real-time monitoring of the engine operation process. During the test, the engine is placed horizontally on a test bench in an open space with ambient flow pressure and temperature conditions. The JetA-1 fuel is used to fire the engine at pre-defined throttles of 20–100%, corresponding to inflow air mass flowrates of 0.134–0.458 kg/s at engine inlets that are recorded for the CFD boundary condition setup later. The gas mixture temperature at the exhaust is measured at around 800 °C at 100% throttle, in agreement with engine design parameters.

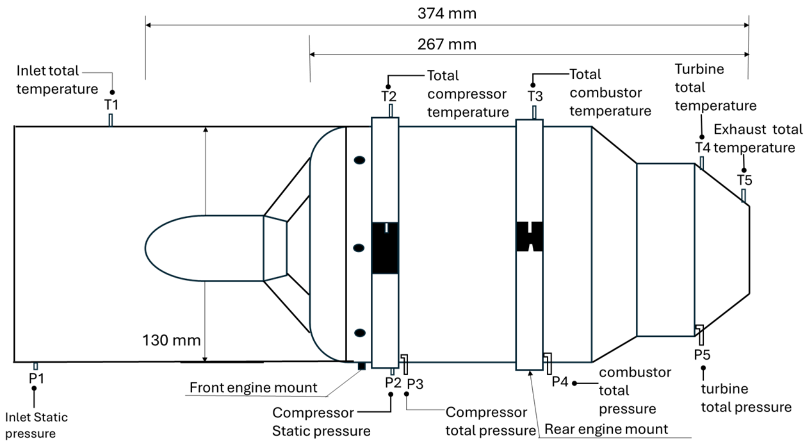

Figure 1. A sketch of the Armfield CM14 gas turbine engine with sensor points (not to scale).

A computer equipped with a data acquisition software system is used to collect test data, transmitted by the engine's built-in pressure sensor and temperature sensor, to measure key results, such as thrust, air and fuel flowrates, pressure and temperature distributions at the AIP face, engine rotating speed, etc. The temperature sensors used are K-type thermocouples and the accuracy is typically a maximum of ±2.2 °C or ±0.75%, whichever is greater. The pressure sensor is a pressure transducer (gauge pressure), and its typical accuracy is ±0.25% FS (full scale). In addition, there are strain gauge load cells with a typical accuracy of ±0.25% FS (full scale). In particular, the engine inlet pressure is measured using a single built-in pressure sensor at the AIP face, located 4 mm before the compressor entry. These data will be used later for validating CFD predictions at the same location.

The original CM14 engine has an intake with a flat lip at the entrance, and key geometry parameters are listed in Table 1, along with a graphical view shown in Figure 2. To reduce geometry effects on flow distortions downstream, the flat lip entrance is replaced by a custom-fabricated intake with a bell-mouth round lip, designed and manufactured at the University of the West of England (UWE) Bristol by Pardo [22] (see Figure 3). Table 1 also provides key parameters of this bell-mouth round lip design. Due to the manufacturing tolerance of 3D printing, a small difference of 1.70 mm in duct diameter was observed between the flat lip and bell-mouth round lip. These two layouts are further studied by CFD to investigate the effect of intake geometrical changes on downstream flow distortions at angled flow velocity conditions of 0–30° and 35 m/s or 70 m/s, respectively.

Table 1. Dimensions of CM14 intake with a flat lip and bell-mouth round lip.

Parameter	Intake with Flat Lip	Intake with Bell-Mouth Round Lip
Outer Ring Diameter (mm)	141.72	150.5
Inner Ring Diameter (mm)	79.8	86.5
Exit Diameter (mm)	88.2	86.5
Intake Length (mm)	304	304
Intake Wall Thickness (mm)	2.45	2.8

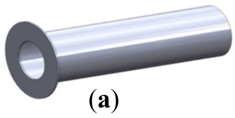

(**a**)

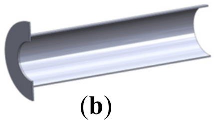

(**b**)

Figure 2. Original intake. (**a**) Injection nozzle with flat lip; (**b**) half a nozzle with inner geometry shape.

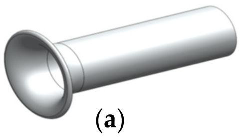

(**a**)

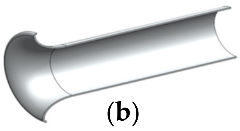

(**b**)

Figure 3. Bell-mouth intake. (**a**) Injection nozzle with round lip; (**b**) half a nozzle with inner geometry shape.

2.2. Inlet Pressure Distortion Descriptors

There are two types of descriptors used to quantify inlet pressure distortions. One commonly used in the UK and Europe is named DC60 Descriptor (distortion coefficient up to 60° range), and the other is the SAE ARP 1420 gas turbine engine inlet flow distortion guidelines mainly used in the USA [9]. The distortion coefficient DC60 is widely used in many major R&D programmes for aircraft engine development [23,24] to determine the degree of engine inlet pressure distortion up to the 60° range along the circumferential direction at the AIP face, ahead of and close to the fan/compressor faces. The formula of DC60 can be expressed as follows [18]:

$$DC60 = \frac{P_{L60} - P_{F,AV}}{P_{DI}}$$

where P_{L60} represents the averaged pressure over the most distorted flow range up to the 60° range, and $P_{F,AV}$ represents the face-averaged pressure over a full annular (360°) range, both at the AIP surface upstream of the fan/compressor entry. P_{DI} is the averaged dynamic pressure at the AIP face of the engine inlet.

Therefore, the DC60 distortion coefficient gives a ratio of the difference between the averaged pressure of the most distorted region up to 60° along the circumferential direction and the averaged pressure at a full circumference direction (360°) at the AIP face to the averaged dynamic pressure at the engine inlet (or its alternative, e.g., engine intake).

2.3. Numerical Method

CFD simulation was carried out by solving the Reynolds-Averaged Navier–Stokes (RANS) governing equations, based on the fundamental principles of mass, momentum, and energy conservation, together with turbulence models. Note that no combustion will be considered as this study is merely focusing on air intake flow of the considered engine. The general mass conservation equation is expressed as follows (see [25]):

$$\frac{\partial \rho}{\partial t} + \nabla \cdot \left(\rho \vec{V} \right) = 0$$

where ρ is density, t is time and $\vec{V}$ is the velocity vector.

The momentum conservation equation is expressed as follows (see [25]):

$$\frac{\partial}{\partial t}\left(\rho \vec{V} \right) + \nabla \cdot \left(\rho \vec{V} \vec{V} \right) = -\nabla p + \nabla \cdot (\overline{\overline{\tau}}) + \rho \vec{g} + \vec{F}$$

where p is static pressure, $\overline{\overline{\tau}}$ is the stress tensor, and $\rho \vec{g}$, $\vec{F}$ are gravity body force and external forces, respectively. The stress tensor is given by

$$\overline{\overline{\tau}} = \mu \left[\left(\nabla \vec{V} + \nabla \vec{V}^{T} \right) - \frac{2}{3} \nabla \cdot \vec{V} I \right]$$

The energy conservation equation is expressed as follows (see [25]):

$$\frac{\partial}{\partial t}(\rho E) + \nabla \cdot \left(\vec{V}(\rho E + p) \right) = \nabla \cdot (k \nabla T) - \nabla \cdot \left(\sum_j h_j J_j \right) + S_h$$

where E is the total energy, T is the static temperature, J_j is the diffusion flux of species j, and S_h is the energy source term. k and h_j are heat flux and diffusion flux coefficients, respectively.

Menter's Shear Stress Transport (*SST*) turbulence model was employed using the k-ω model to solve turbulent flow in the near-wall region and the standard k-ε model for turbulent flow away from the wall. The equations of the SST turbulence model are illustrated below (see [25,26]).

The turbulence kinetic energy, k, can be expressed as

$$\frac{\partial}{\partial t}(\rho k) + \frac{\partial}{\partial x_i}(\rho k u_i) = \frac{\partial}{\partial x_j}\left(\Gamma_k \frac{\partial k}{\partial x_j} \right) + G_k - Y_k + S_k$$

where G_k represents the generation of turbulence kinetic energy due to the mean velocity gradients, and Y_k represents the dissipation of k due to turbulence. S_k is the user-defined source term. Γ_k represents the effective diffusivity of k.

The turbulence dissipation rate, ω, is represented as

$$\frac{\partial}{\partial t}(\rho \omega) + \frac{\partial}{\partial x_i}(\rho \omega u_i) = \frac{\partial}{\partial x_j}\left(\Gamma_\omega \frac{\partial \omega}{\partial x_j} \right) + G_\omega - Y_\omega + D_\omega + S_\omega$$

where G_ω represents the generation of ω. Γ_ω represents the effective diffusivity of ω. Y_ω represents the dissipation of ω due to turbulence. D_ω represents the cross-diffusion term. S_ω is the user-defined source term.

The finite volume (FV) method was used to discretise the above governing equations. Unsteady (transient) flow simulations were carried out until a statistically converged status was achieved, judged by key indicators such as time history of normal/axial forces.

3. Computational Domain, Boundary Conditions and Mesh Convergence Study

Figure 4 illustrates a two-dimensional (2D) cross section derived from a centre plane of the three-dimensional (3D) fluid domain employed in CFD simulations. The geometry of intake configurations and sizes for both the flat lip (named as case 1 hereafter) and the bell-mouth round lip (named as case 2 hereafter) are replicated to match those deployed for the experimental tests using the Armfield CM14 microjet gas turbine engine (see Figure 4). The computational domain diameter (i.e., height in 2D view) is defined as 837.44 mm (i.e., about 5.2–5.9 times the intake ring outer diameter), and the domain length is set to 912 mm (i.e., 3 times the intake duct length) for both case 1 and case 2.

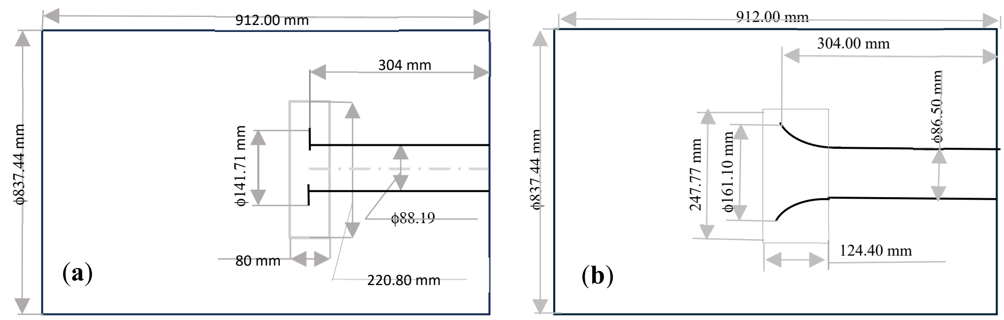

Figure 4. A 2D cross-section plane of 3D CFD domain (not to scale). (**a**) Case 1—flat lip; (**b**) case 2—bell-mouth round lip.

To compare experimental tests, pressure far-field conditions are applied for the inlet plane, upper/lower boundaries and outlet plane outside the duct exit. At the duct exit, mass flowrates from the test measurement are used, and they correspond to throttles of 20–100%. Non-slip conditions are applied for all walls (interior and exterior of the intake entrance and the duct tube).

For the CFD study of angled inflow velocity, inflow velocities of 35 m/s and 70 m/s are applied at an incident angle between 0 and 30°. The mass flowrate corresponding to 100% throttle is used at the duct exit, and other boundary conditions remain the same as ambient inflow simulations with the pressure far-field condition.

CFD computational domains were discretised by using the polyhedral meshing method (see Figures 5 and 6). A body of influence was applied for an enclosure surrounding the intake with a diameter of 220.80 mm and a length of 80 mm for the flat lip (case 1) and a diameter of 247.77 mm and a length of 124.40 mm for the bell-mouth round lip (case 2). This is to enhance the mesh resolution and quality around the intake entrance section and its near-wall regions. A total of 11 computational meshes (i.e., 6 for flap lip intake, 5 for bell-mouth round lip intake; see Tables 2 and 3) are generated with high quality, i.e., skewness of 0.02943–0.0324 and orthogonality of 0.968–0.972, respectively.

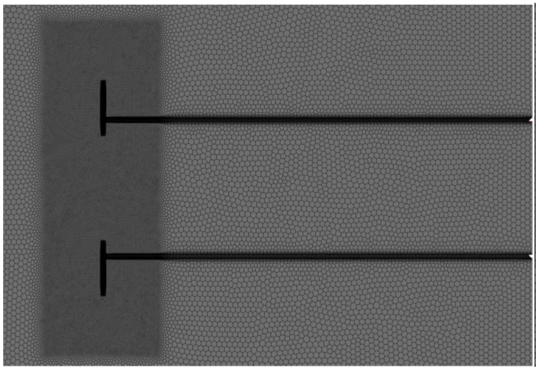

(**a**) Mesh in cross-section plane.

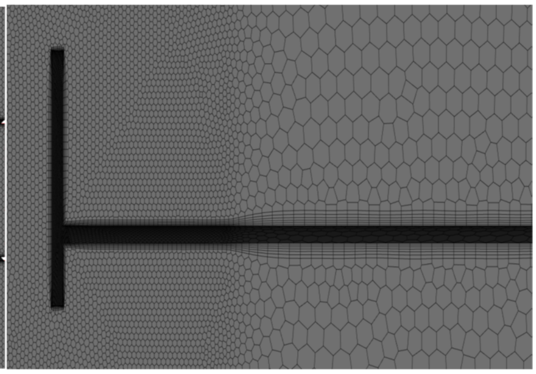

(**b**) Mesh around flat lip.

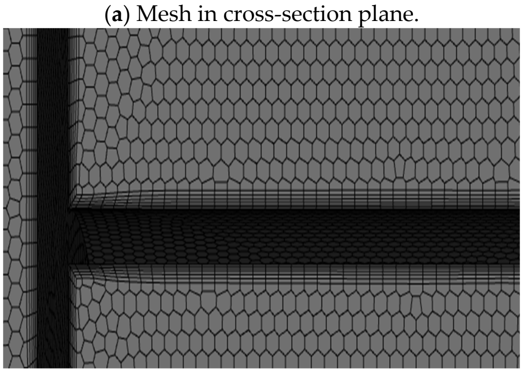

(**c**) Closed view of meshes around flat lip.

Figure 5. Polyhedral meshes at cross-section plane for 3D intake with flat lip.

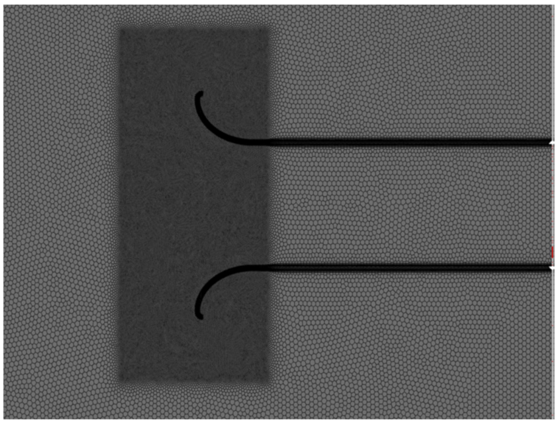

(**a**) Mesh in cross-section plane

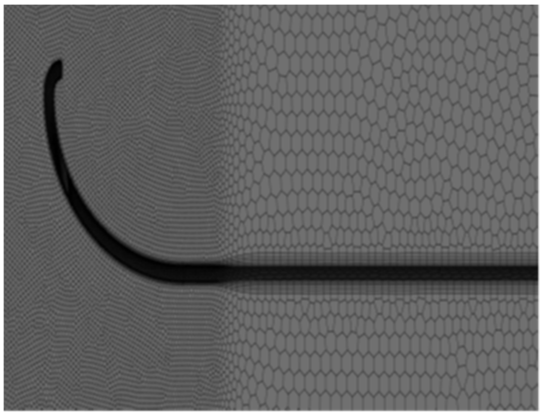

(**b**) Mesh around bell-mouth round lip.

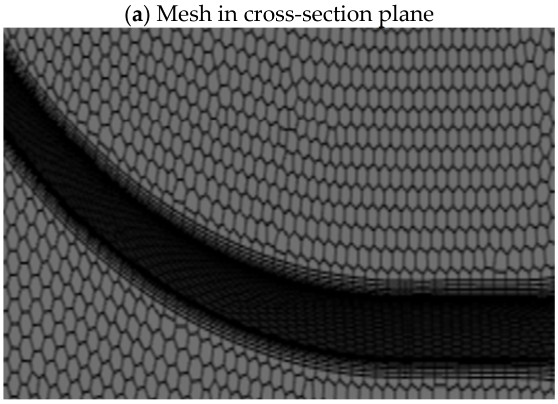

(**c**) Closed view of meshes around bell-mouth round lip.

Figure 6. Polyhedral mesh at cross-section plane for 3D intake with bell-mouth round lip.

Table 2. Mesh convergence study for the intake with a flat lip.

Mesh Set	Mesh Element	Pressure (10^4 Pa) CFD [1*]	Pressure (10^4 Pa) Experiment [2*]	Percentage Error %	Skewness	Orthogonality
1	3.568×10^6	−1.436	−1.459	1.580	0.0296	0.970
2	4.320×10^6	−1.450	−1.459	0.617	0.0296	0.970
3	4.640×10^6	−1.450	−1.459	0.617	0.0324	0.968
4	5.710×10^6	−1.453	−1.459	0.411	0.0310	0.969
5	7.880×10^6	−1.450	−1.459	0.617	0.0305	0.970
6	8.997×10^6	−1.452	−1.459	0.480	0.0320	0.968

[1*] CFD data are taken at the AIP face at ambient conditions during the test. The pressures are static gauge values.
[2*] Experimental data measured at the AIP face at 100% throttle operation conditions.

Table 3. Mesh convergence study for the intake with the bell-mouth round lip.

Mesh Set	Mesh Element	Pressure (10^4 Pa) CFD [1*]	Pressure (10^4 Pa) Experiment [2*]	Percentage Error %	Skewness	Orthogonal
1	6.093×10^6	−2.497	−2.614	4.480	0.0297	0.970
2	6.373×10^6	−2.505	−2.614	4.170	0.0298	0.970
3	6.828×10^6	−2.502	−2.614	4.290	0.0294	0.971
4	8.443×10^6	−2.504	−2.614	4.210	0.0293	0.971
5	10.76×10^6	−2.504	−2.614	4.210	0.0276	0.972

[1*] CFD data are taken at the AIP face at ambient conditions during the test. The pressure is static gauge values.
[2*] Experimental data measured at the AIP face at 100% throttle operation conditions.

CFD simulation starts with a baseline study by using ambient inflow conditions (i.e., pressure far-field conditions) and the experimental mass flowrate at the duct exit, and CFD-predicted static (gauge) pressure at the AIP face is collected for comparison with experimental test data (see Tables 2 and 3). For the flap lip intake (case 1), the percentage errors (%) between CFD prediction and test data are between 0.411% and 1.58%, and for the bell-mouth round lip intake (case 2), the percentage errors are slightly high, between 4.17% and 4.48%, respectively. Based on mesh convergence study results, it was decided to choose mesh 4 (i.e., 5.710 million cells) for further case 1 study and mesh 4 (i.e., 8.443 million cells) for further case 2 study, at different throttle conditions.

Figure 7 presents the CFD-predicted static (gauge) pressure at the AIP face from 11 computational meshes with different numbers of mesh elements (see Table 2 for case 1, and Table 3 for case 2). For case 1 intake with a flat lip, the pressure varies with the increase in the number of mesh cells initially, and then it starts to stabilise for two meshes with 4.32×10^6 and 5.710×10^6 cells with very small deficiencies between 0.617% and 0.411%, compared to experimental data at 100% throttle (see Table 2). The percentage of error rebounds slightly for two finer meshes of 7.880×10^6 and 8.997×10^6. It was decided to use 5.71×10^6 mesh cells for further CFD simulations. For case 2 intake with a bell-mouth round lip, the predicated pressure at the AIP face stays almost constant (see Figure 7b). The discrepancies between CFD predictions and experimental measurements are 4.49%, 4.18%, 4.33%, and 4.22% (see Table 3), respectively. Therefore, it was decided to adopt 8.443×10^6 mesh cells for further CFD studies.

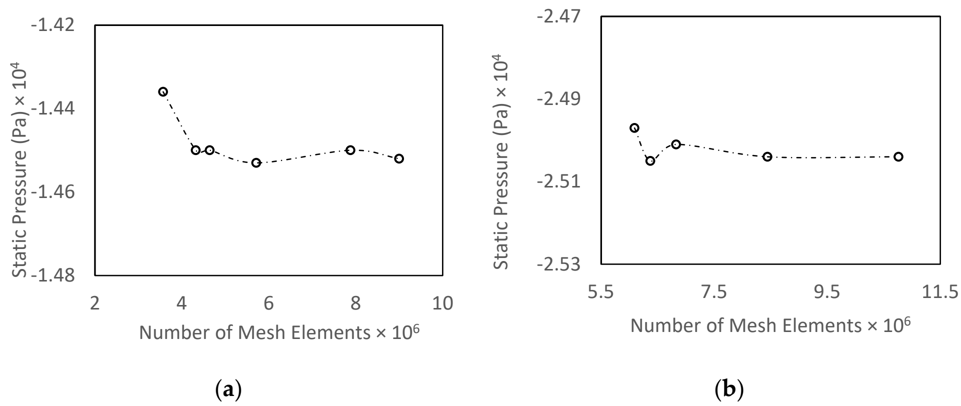

Figure 7. CFD-predicted static gauge pressure variation with number of mesh elements at 100% engine throttle and ambient conditions. (**a**) Case 1—flat lip; (**b**) case 2—bell-mouth round lip.

4. Results and Discussion

4.1. Variation in Static Gauge Pressure with Throttle at Ambient Conditions

At ambient inflow conditions and applying experimental mass flowrates at the duct exit, CFD-predicted static pressure ratios (normalised by ambient pressure of 1 atm) are compared with experimental data taken at the AIP face for both flat lip and bell-mouth round lip intakes (see Figure 8). A trend of static pressure decreasing monotonically with an increase in throttle conditions from 20% to 100% is illustrated. This indicates that the engine inlet pressure distortion increases due to non-uniformly distributed airflow entering the downstream fan/compressor stage, causing a reduction in engine performance. CFD predictions are found to be in good agreement with the experimental test data, especially for the flat lip in case 1. It is also noted that the engine inlet pressure distortion level from the intake with a flat lip (see Figure 8a) is more severe than that from the intake with a bell-mouth round lip (see Figure 8b). The averaged standard deviations of static pressure ratios are about 0.214% for case 1 and 0.097% for case 2 when comparing CFD predictions with experimental data.

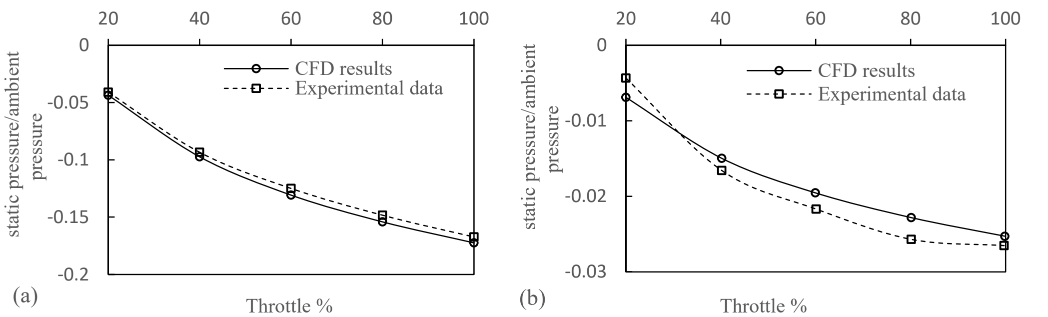

Figure 8. The ratio of averaged static gauge pressure and ambient pressure at the AIP face as a function of throttle. Comparison of the experimental data and CFD results: (**a**) flat lip (case 1); (**b**) bell-mouth round lip (case 2).

4.2. Intake with Flat Lip at 100% Throttle Conditions

For the intake with a flat lip, instantaneous flow behaviours from CFD simulation are depicted by plotting static gauge pressure contours at seven inflow incident angles ranging from 0° to 30° at an increment of 5° and two inflow velocity conditions of 35 m/s and 70 m/s. Figure 9 shows the non-uniform distributions of static pressure while changing the incoming airflow angle from 0° to 30°, with a distinct and dominant lower-pressure region and higher-pressure region, respectively. Due to large differences in the flow field, different legends are used to distinguish lower- and higher-pressure regions.

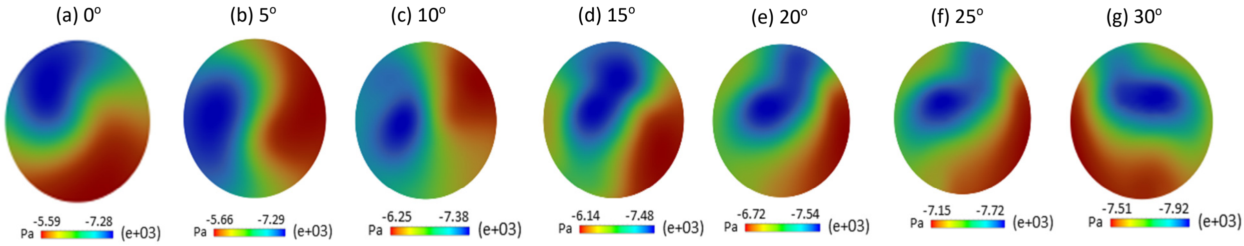

Figure 9. Pressure contours at the AIP face with flat lip intake at various inflow angles and a velocity of 35 m/s.

At a low incoming speed of 35 m/s, the cores of lower-pressure and higher-pressure regions move anticlockwise initially with the increase in incident angles from 0° to 10°, and later rotate clockwise from an incident angle of 15° to 30°. By doubling the incoming velocity to 70 m/s, two distinct lower- and higher-pressure regions still exist, but with different distribution patterns and movements observed (see Figure 10). It is noted that while increasing the inflow angle from 0° to 5°, the flow pattern changes from a ring type to two separate regions. Similar patterns remain until an inflow angle of 15°, and at three higher inflow angles of 20°, 25° and 30°, the lower- and higher-pressure regions oscillate in the vertical direction, indicating large-scale flow movements.

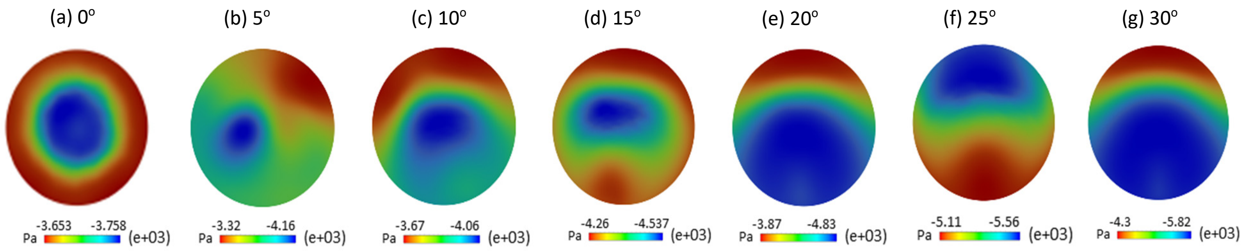

Figure 10. Pressure contours at the AIP face with flat lip intake at various inflow angles and a velocity of 70 m/s.

For the intake with a bell-mouth round lip, clear and persistent pressure distributions (Figure 11) can be seen at a low inflow velocity of 35 m/s, and the overall patterns remain more or less the same, indicating that it is less influenced by the inflow incident angle increase. Unlike the flat lip intake case, the lower-pressure region (in blue) always resides in the central area of the intake, while the higher-pressure region around the edge of the duct ring is circumferential with some degree of variation. While increasing the inflow velocity to 70 m/s (see Figure 12), a similar pattern appears at a 0° incident angle. However, when the incident angle increases to 5–25°, this pattern dramatically changes, with higher-pressure regions (in blue) appearing around the edge of the ring circumferentially along with a few patches of the lower-pressure regions (in red). At the highest incident angle of 30°, the pressure distributions appear to be quite similar, as seen from a low flow velocity of 35 m/s at the same incident angle. These observations are qualitatively in agreement with other researchers, e.g., Reddy and Subramanian [27] and Tiwari et al. [28], who concluded that a bell-mouth inlet design can lead to highly uniform flow distributions and thus minimise the pressure losses associated with flow that is fully attached to the wall surfaces. Reddy further argued that bell-mouth designs could reduce boundary-layer thickness and flow angularity [27] which could be another reason for the low flow distortion at the AIP face ahead of the compressor entry.

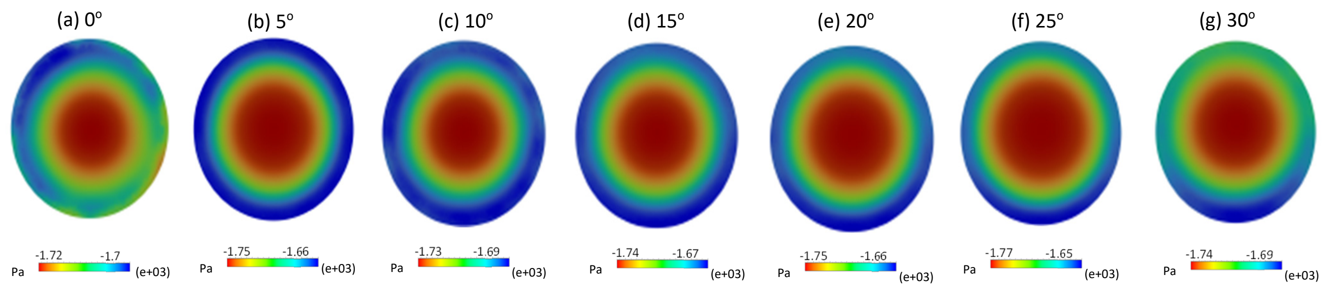

Figure 11. Pressure contours at the AIP face with a bell-mouth round lip intake at various inflow angles and a velocity of 35 m/s.

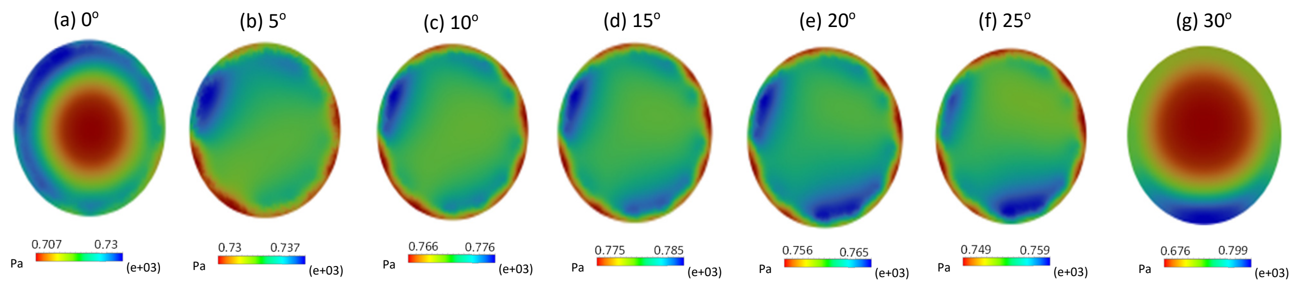

Figure 12. Pressure contours at the AIP face with a bell-mouth round lip intake at various inflow angles and a velocity of 70 m/s.

4.3. Static Pressure Distortions with 100% Throttle Conditions at Various Inflow Angles

As previously mentioned, the discharge coefficient DC60 is a value used to measure the pressure loss along the circumference direction up to a 60° range at the AIP face of the engine inlet, where the pressure loss is the most severe [19].

Based on CFD simulation results for two inflow velocities of 35 m/s and 70 m/s, Figure 13 gives the CFD-predicted pressure loss in terms of DC60 as a function of the inflow incident angle ranging from 0° to 35°. It is clear that both inflow angle and inflow velocity influence the engine inlet pressure distortions to some extent. For the intake with a flat lip (Figure 13a), the inflow velocity has less of an effect on DC60 predictions between the inflow angles of 0 and 15°, illustrated by two DC60 curves that show a similar trend and are close to each other. Beyond an incident angle of 15°, DC60 curves are diverted with a rapid steep decrease at the inflow velocity of 70 m/s, reaching a value of −1.2 at a 30° angle, and a relatively slower decrease for the inflow velocity of 35 m/s, reaching a value of −0.5 at a 30° angle. Compared to DC60 at zero inflow angle, it reduces by a factor of about 3 for the low velocity of 35 m/s and by a factor of 20 for the high velocity of 70 m/s. For intake with a bell-mouth round lip, DC60 shows little variations just below zero at a low velocity of 35 m/s. By doubling the incoming velocity to 70 m/s, DC60 shows non-zero values but with small magnitudes around 0.03 at the inflow angle of 0°, then shifts upwards towards zero at the inflow angle of 15°, and after this, it drifts downwards with small negative values (see Figure 13b). Overall, DC60 from the bell-mouth round lip intake is much smaller compared to the flat lip intake. These findings are consistent with a previous study by Pe˘cinka et al. [19], who used a round lip intake configuration with a distortion screen to investigate flow distortion at the engine inlet. Cao et al. [16] also captured the same tendency of DC60: the pressure ratio declines with an increase in the incident angle and mass flowrate of fluids through the intake entrance [16].

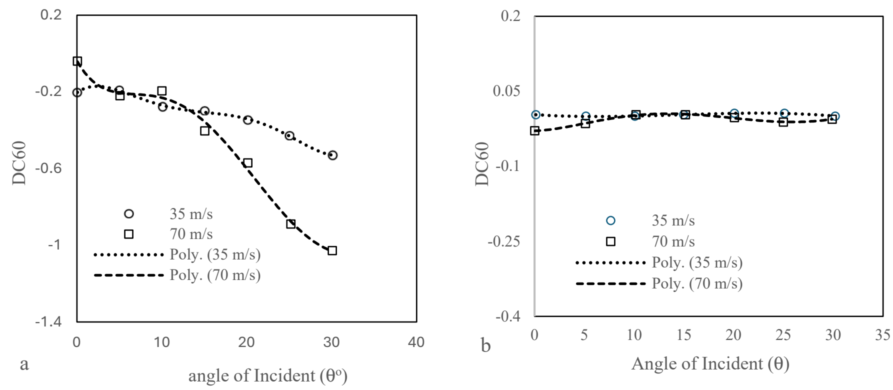

Figure 13. Comparison of distortion coefficient DC60 at the AIP face with two inflow velocities and various inflow angles from 0° to 30°. (**a**) Intake with flat lip; (**b**) intake with bell-mouth round lip.

Further data analysis is performed by correlating data points using polynomial curve fitting with a mean square R value close to 1 for both case 1 and case 2, as seen from eqns. (1–4) below. They indicate that the curve fittings are accurate up to the fifth order for case 1 (flat lip) with inflow velocities of 35 m/s and 70 m/s and for case 2 (bell-mouth round lip) with the inflow velocity of 70 m/s, and they are accurate up to the third order for case 2 with an inflow velocity of 35 m/s. The following depicts the four correlation equations for both case 1 and case 2.

(1) Case 1 with flat lip intake

Inflow velocity at 35 m/s:

$$y = 4 \times 10^{-7}\chi^5 - 3 \times 10^{-5}\chi^4 + 0.0008\chi^3 - 0.0093\chi^2 + 0.0322\chi - 0.2048 \ (R^2 = 0.9985) \quad (1)$$

Inflow velocity at 70 m/s:

$$y = -3 \times 10^{-7}\chi^5 + 3 \times 10^{-5}\chi^4 - 0.001\chi^3 + 0.0132\chi^2 - 0.0783\chi - 0.0374 \ (R^2 = 0.9937) \quad (2)$$

(2) Case 2 with bell-mouth round lip intake

Inflow velocity at 35 m/s:

$$y = -3 \times 10^{-6}\chi^3 + 0.0001\chi^2 - 0.0014\chi + 0.0033 \ (R^2 = 0.9874) \quad (3)$$

Inflow velocity at 70 m/s:

$$y = -2 \times 10^{-8}\chi^5 + 2 \times 10^{-6}\chi^4 - 7 \times 10^{-5}\chi^3 + 0.0008\chi^2 + 0.0006\chi - 0.0292 \ (R^2 = 0.9949) \quad (4)$$

5. Conclusions

A computational fluid dynamics study has been performed to investigate the effects of inflow angle and magnitude changes on pressure distortions at the AIP face ahead of the fan/compressor entry of a microjet gas turbine engine CM14. For both flat lip and bell-mouth round lip intakes, CFD-predicted static pressures are in good agreement with experimental test data at 20–100% throttle conditions, at the same operation conditions as the engine tests. The CFD study continues at angled inflow velocities of 35 m/s and 70 m/s, respectively, to investigate geometrical changes in engine inlet pressure distortion using distortion coefficient DC60.

For the intake with a flat lip entry, the CFD results show a clear trend between the distortion magnitude and the inflow incident angle. It was found that the engine inlet experiences more severe flow distortions while the inflow angle increases, in good agreement with the findings of Cao et al. [16]. The engine inlet pressure distortions are significantly intensified at the AIP face while the inflow incident angle is greater than 15° and reaches the maximum value at 30° for both inflow velocities (35 m/s, 70 m/s) adopted for the CFD simulation. For the intake with a bell-mouth round lip entry, engine inlet pressure distortion is found to be less severe compared to the intake with a flat lip entry, and the distortion magnitudes remain at small values with an increase in the inflow incident angle. This is reflected by static gauge pressure contours which show a more uniform distribution of pressure distributions at the AIP face and gradual changes in pressure along the circumferential direction. The dynamic flow behaviour shows that the majority of the flow attaches to the intake walls until it reaches the downstream engine fan/compressor entry. In comparison, the pressure distributions from the intake with a flat lip entry are more randomly distributed at the AIP face.

The higher pressure distortion due to the increase in the inflow incident angle is likely attributed to the incoming flow turbulence and flow separation at the intake entry and along the duct walls, therefore provoking more non-uniform flow stream while reaching the downstream engine fan/compressor entry. This will lead to strong unsteady flow motions and large pressure variations that can result in potential damage to the engine. In conclusion, the intake entry configuration can have a major impact on overall engine performance. Therefore, it requires careful design, testing and evaluation. Future work includes CFD simulations over wider design parameters and flow conditions, and the use of machine learning to improve the efficiency and accuracy of prediction, data mining and analysis.

Author Contributions: Conceptualization, J.Y. and B.C.; methodology, J.Y. and Y.Y.; validation, S.S.V., J.Y. and B.C.; formal analysis, S.S.V. and J.Y.; investigation, S.S.V. and J.Y.; resources, B.C. and Y.Y.; data curation, S.S.V. and J.Y.; writing—original draft preparation, S.S.V. and J.Y.; writing—review and editing, Y.Y. and B.C.; visualization, S.S.V. and J.Y.; supervision, J.Y.; project administration, Y.Y. All authors have read and agreed to the published version of the manuscript.

Funding: This research received no external funding.

Data Availability Statement: The data presented in this study are available on request from the corresponding author.

Conflicts of Interest: The authors declare no conflict of interest.

References

1. Doll, U.; Migliorini, M.; Baikie, J.; Zachos, P.K.; Roehle, I.; Melnikov, S.; Steinbock, J.; Dues, M.; Kapulla, R.; MacManus, D.G.; et al. Non-intrusive flow diagnostics for unsteady inlet flow distortion measurements in novel aircraft architectures. *Prog. Aerosp. Sci.* **2022**, *130*, 100810. [CrossRef]
2. Drela, M. Development of the D8 transport configuration. In Proceedings of the AIAA Paper 2011-3970, the 29th AIAA Applied Aerodynamics Conference, Honolulu, HI, USA, 27–30 June 2011.
3. Naseri, A.; Sammak, S.; Boroomand, M.; Alihosseini, A.; Tousi, A.M. Experimental Investigation of Inlet Distortion Effect on Performance of a Micro Gas Turbine. *J. Eng. Gas Turbines Power* **2018**, *140*, 092604. [CrossRef]
4. Tanguy, G.; MacManus, D.G.; Garnier, E.; Martin, P.G. Characteristics of Unsteady Total Pressure Distortion for a Complex Aero-engine Intake Duct. *Aerosp. Sci. Technol.* **2018**, *78*, 297–311. [CrossRef]
5. Zachos, P.K.; MacManus, D.G.; Gil-Prieto, D.; Chiereghin, N. Flow Distortion Measurements in Convoluted Aero Engine Intakes. *AIAA J.* **2016**, *54*, 2819–2832. [CrossRef]
6. Gil-Prieto, D.; MacManus, D.G.; Zachos, P.K.; Tanguy, G.; Menzies, K.R. Convoluted intake distortion measurements using stereo particle image velocimetry. *AIAA J.* **2017**, *55*, 1878–1892. [CrossRef]
7. Rademakers, R.P.M.; Bindl, S.; Niehuis, R. Effects of Flow Distortions as They Occur in S-Duct Inlets on the Performance and Stability of a Jet Engine. *J. Eng. Gas Turbines Power* **2016**, *138*, 022605. [CrossRef]
8. MacManus, D.G.; Chiereghin, N.; Prieto, D.G.; Zachos, P. Complex Aeroengine Intake Ducts and Dynamic Distortion. *AIAA J.* **2017**, *55*, 2395–2409. [CrossRef]

9. Seddon, J.; Goldsmith, E. *Intake Aerodynamics*; AIAA Education Series; AIAA: Reston, VA, USA, 1999.
10. Sivapragasam, M. Numerical and experimental investigation on flow distortion in an aero engine air intake. *SASTECH J. MSRSAS* **2007**, *6*, 28–35.
11. Hodder, B.K. An Investigation of Engine Influence on Inlet Performance. NASA CR-166136. 1981. Available online: https://ntrs.nasa.gov/api/citations/19810021546/downloads/19810021546.pdf (accessed on 1 February 2025).
12. Kennedy, S.; Robinson, T.; Spence, S.; Richardson, J. Computational Investigation of Inlet Distortion at High Angles of Attack. *J. Aircr.* **2014**, *51*, 361–376. [CrossRef]
13. Carnevale, M.; Wang, F.; Green, J.S.; Di Mare, L. Lip Stall Suppression in Powered Intakes. *J. Propuls. Power* **2015**, *32*, 161–170. [CrossRef]
14. Iek, C.; Boldman, D.R. 3-D Viscous Flow CFD Analysis of the Propeller Effect on an Advanced Ducted Propeller Subsonic Inlet. In Proceedings of the 29th Joint Propulsion Conference and Exhibit, Monterey, CA, USA, 28–30 June 1993; NASA Technical Memorandum 106240. AIAA-93-1847. Available online: https://ntrs.nasa.gov/api/citations/19930019973/downloads/19930019973.pdf (accessed on 1 February 2025).
15. Peters, A.; Spakovszky, Z.S.; Lord, W.K.; Rose, B. Ultrashort Nacelles for Low Fan Pressure Ratio Propulsors. *J. Turbomach.* **2015**, *137*, 021001. [CrossRef]
16. Cao, T.; Vadlamani, N.R.; Tucker, P.G.; Smith, A.R.; Slaby, M.; Sheaf, C.T.J. Fan–Intake Interaction Under High Incidence. *J. Eng. Gas Turbines Power* **2016**, *139*, 041204. [CrossRef]
17. Hodder, B.K.; Farquhar, B.; Dudley, M. A large-scale investigation of engine influence on inlet performance at angle-of-attack. In Proceedings of the 1st Flight Test Conference, Las Vegas, NV, USA, 11–13 November 1981.
18. Boldman, D.R.; Iek, C.; Hwang, D.P. Effect of a Rotating Propeller on the Separation Angle of Attack and Distortion in Ducted Propeller Inlets. In Proceedings of the Aerospace Sciences Meeting and Exhibit, Reno, NV, USA, 11–13 January 1993. NASA TM-105935.
19. Pecinka, J.; Bugajski, G.T.; Kmoch, P.; Jilek, J. Jet Engine Inlet Distortion Screen and Descriptor Evaluation. *Acta Polytech.* **2017**, *57*, 22–31.
20. Armfield Jet Engine Instruction Manual CM14, Issue 12, October 2015. Available online: https://armfield.co.uk/product/cm14-axial-flow-gas-turbine/ (accessed on 1 February 2025).
21. Olympus HP e-Start Data Sheet, AMT Netherlands. 2020. Available online: https://www.amtjets.com/pdf/Olympus-HP-in-University-config-feb-2020.pdf (accessed on 1 February 2025).
22. Pardo, J. Design, Manufacturing & Implementation of a Bellmouth Intake on the CM14 Turbojet. Master's Thesis, University of the West of England Bristol, Bristol, UK, 2023.
23. Bissinger, C.; Breuer, N.T. *Basic Principles—Gas Turbine Compatibility—Intake Aerodynamic Aspects*; Book section EAE487; John Wiley and Sons: Hoboken, NJ, USA, 2010; Volume 8.
24. Kurzke, J. Effects of inlet flow distortion on the performance of aircraft gas turbine. *J. Eng. Gas Turbines Power* **2008**, *130*, 041201. [CrossRef]
25. *ANSYS Fluent Theory Guide*; ANSYS, Inc.: Canonsburg, PA, USA, 2006.
26. Carcangiu, C.E. CFD-RANS Study of Horizontal Axis Wind Turbines. Ph.D. Thesis, Università di Cagliari, Cagliari, Italy, 2008. Available online: https://iris.unica.it/handle/11584/266029 (accessed on 1 February 2025).
27. Reddy, H.; Subramanian, B. Aerodynamic Design of Three-Dimensional Bellmouth for Low-Speed Open-Circuit Wind Tunnel. *Int. J. Aerosp. Mech. Eng.* **2022**, *16*, 241–255.
28. Tiwari, A.; Lad, A.; Patel, S.; Mistry, C.S. Development of Bell Mouth for Low-speed Axial Flow Compressor Testing Facility. In Proceedings of the Asian Congress on Gas Turbines, Mumbai, India, 14–16 November 2016; Tiwari, A., Ed.; ACGT2016-18.